

# Complex-coordinate non-Hermitian transformation optics

S Savoia, G Castaldi and V Galdi

Waves Group, Department of Engineering, University of Sannio, Benevento, I-82100, Italy

E-mail: [vgaldi@unisannio.it](mailto:vgaldi@unisannio.it)

Received 22 September 2015, revised 5 December 2015

Accepted for publication 8 December 2015

Published 1 April 2016



## Abstract

Transformation optics (TO) is conventionally based on *real-valued* coordinate transformations and, therefore, cannot naturally handle metamaterials featuring gain and/or losses. Motivated by the growing interest in *non-Hermitian* optical scenarios featuring spatial modulation of gain and loss, and building upon our previous studies, we explore here possible extensions of the TO framework relying on *complex-valued* coordinate transformations. We show that such extensions can be naturally combined with well-established powerful tools and formalisms in electromagnetics and optics, based on the ‘complexification’ of spatial and spectral quantities. This enables us to deal with rather general non-Hermitian optical scenarios, while retaining the attractive characteristics of conventional (real-valued) TO in terms of physically incisive modeling and geometry-driven intuitive design. As representative examples, we illustrate the manipulation of beam-like wave-objects (modeled in terms of ‘complex source points’) as well as radiating states (‘leaky waves’, modeled in terms of complex-valued propagation constants). Our analytical results, validated against full-wave numerical simulations, provide useful insight into the wave propagation in non-Hermitian scenarios, and may indicate new directions in the synthesis of active optical devices and antennas.

Keywords: metamaterials, transformation optics, non-Hermitian optics, parity-time symmetry

(Some figures may appear in colour only in the online journal)

## 1. Introduction

In the synthesis of metamaterials, the use of material constituents featuring gain is a well-established strategy to overcome the inevitable presence of losses, so as to attain effectively lossless (or active) implementations [1]. Besides this more or less obvious scenario, recent studies have provided theoretical, numerical and experimental evidence of a wealth of anomalous effects and interactions associated with judicious spatial modulation of loss and gain, including double refraction [2], spectral singularities [3], spontaneous symmetry breaking and power oscillations [4], unidirectional invisibility [5, 6], coherent perfect absorption [7, 8], negative refraction and focusing [9], and bound states in the continuum [10], just to mention a few. This has generated considerable interest in exploring a variety of related potential applications to optical and plasmonic scenarios including e.g. cavities [11, 12], lasers [13], couplers [14], switches [15], isolators [16], invisibility cloaks [17, 18], metamaterials [19, 20],

tunneling and waveguiding [21–23], composite dielectric/magnetic structures [24], and topological photonic structures [25, 26].

Based on the formal analogy between classical optics and quantum mechanics, most of the above studies have been triggered and inspired by the *parity-time* ( $\mathcal{PT}$ ) symmetry concept introduced by Bender and co-workers [27–29] as a possible extension of quantum mechanics based on *non-Hermitian*, complex-valued Hamiltonians satisfying suitable symmetry conditions. Accordingly, the general term ‘non-Hermitian optics’ is typically utilized when referring to the above-mentioned optical counterparts. It is worth recalling that certain aspects of the  $\mathcal{PT}$ -symmetric quantum-mechanics extension are still controversial (see e.g. [30–32]), but this does not affect the physical soundness the non-Hermitian optical counterparts.

Within this largely unexplored research area, a systematic and versatile design approach like transformation optics (TO) [33, 34], based on the form-invariance of Maxwell’s and

Helmholtz equations with respect to coordinate transformations, may provide valuable insights and may open up new application scenarios and perspectives. However, due to the inherently *real-valued* character of the underlying coordinate transformations, conventional TO approaches cannot naturally handle ‘transformation media’ characterized by complex-valued constitutive parameters (typical of materials featuring loss or gain), unless these are already present in the auxiliary space to be transformed. One possible TO extension that would allow one to overcome these limitations relies on the analytic continuation of the coordinate transformations to the *complex* plane.

Indeed, the ‘complexification’ of geometrical objects (spatial coordinates, curves, etc) is a well-known concept of longstanding interest in electromagnetics (EM) and optics, with the prominent examples of ‘complex source point’ (CSP) [35, 36], ‘complex rays’ [37, 38], and complex-coordinate-stretching-based absorbing boundary conditions [39]. With specific reference to TO, recent complex-coordinate extensions have been proposed in order to enable field-amplitude control [40], and to generate single-negative [41], and  $\mathcal{PT}$ -symmetric [19] transformation media. Also worthy of mention are very recent applications to reflectionless media [42].

In particular, in [19], we proposed a complex-coordinate TO extension that could naturally handle non-Hermitian optical scenarios. This allows, for instance, the metamaterial-based interpretation (and possible implementation) of complex-coordinates-inspired wave-objects and resonant states, as well as the geometrical interpretation of the  $\mathcal{PT}$ -symmetry concept and the spontaneous symmetry breaking phenomenon in terms of analytic features of the underlying coordinate transformations.

In this paper, we proceed along the same lines, by exploring further examples and application scenarios. In particular, after a brief summary (section 2) of our previous results from [19], we introduce (section 3) a general class of non-Hermitian metamaterial transformation slabs for the manipulation of beam-like wave-objects modeled in terms of CSPs. Moreover, we also explore the manipulation of ‘leaky waves’ (LWs) associated with complex-valued solutions of the dispersion equation of open waveguides. Besides the analytical developments (with some details relegated in four appendices), we also present numerical validations based on full-wave simulations. Finally, we provide some brief concluding remarks and hints for future research (section 4).

## 2. Summary of previous work

For the sake of completeness, we compactly summarize the main results from [19]. As in conventional (real-valued) TO [34], we consider a time-harmonic EM field distribution  $\mathbf{E}'$ ,  $\mathbf{H}'$  (with suppressed  $\exp(-i\omega t)$  time-harmonic dependence) radiated by electric ( $\mathbf{J}'$ ) and magnetic ( $\mathbf{M}'$ ) sources in an auxiliary space with Cartesian coordinates  $\mathbf{r}' \equiv (x', y', z')$  filled by a lossless medium characterized by (real-valued) relative permittivity and permeability distributions  $\varepsilon'(\mathbf{r}')$  and

$\mu'(\mathbf{r}')$ , respectively. By exploiting the form-invariance property properties of Maxwell’s equations, the field/source-manipulation effects induced by a coordinate transformation

$$\mathbf{r}' = \mathbf{F}(\mathbf{r}) \quad (1)$$

can be equivalently attributed to a new set of sources

$$\{\mathbf{J}, \mathbf{M}\}(\mathbf{r}) = \det[\vec{\Lambda}(\mathbf{r})] \vec{\Lambda}^{-1}(\mathbf{r}) \cdot \{\mathbf{J}', \mathbf{M}'\}[\mathbf{F}(\mathbf{r})], \quad (2)$$

radiating a new set of EM fields

$$\{\mathbf{E}, \mathbf{H}\}(\mathbf{r}) = \vec{\Lambda}^T(\mathbf{r}) \cdot \{\mathbf{E}', \mathbf{H}'\}[\mathbf{F}(\mathbf{r})], \quad (3)$$

in a new physical space  $\mathbf{r} \equiv (x, y, z)$  filled up by an inhomogeneous, anisotropic ‘transformation medium’ characterized by relative permittivity and permeability tensors

$$\begin{aligned} \vec{\varepsilon}(\mathbf{r}) &= \varepsilon'[\mathbf{F}(\mathbf{r})] \det[\vec{\Lambda}(\mathbf{r})] \vec{\Lambda}^{-1}(\mathbf{r}) \cdot \vec{\Lambda}^{-T}(\mathbf{r}), \\ \vec{\mu}(\mathbf{r}) &= \mu'[\mathbf{F}(\mathbf{r})] \det[\vec{\Lambda}(\mathbf{r})] \vec{\Lambda}^{-1}(\mathbf{r}) \cdot \vec{\Lambda}^{-T}(\mathbf{r}). \end{aligned} \quad (4)$$

In equations (2)–(4),

$$\vec{\Lambda} \equiv \begin{bmatrix} \frac{\partial x'}{\partial x} & \frac{\partial x'}{\partial y} & \frac{\partial x'}{\partial z} \\ \frac{\partial y'}{\partial x} & \frac{\partial y'}{\partial y} & \frac{\partial y'}{\partial z} \\ \frac{\partial z'}{\partial x} & \frac{\partial z'}{\partial y} & \frac{\partial z'}{\partial z} \end{bmatrix} \quad (5)$$

indicates the Jacobian matrix of the transformation in equation (1), double-headed arrows are used to identify second-rank tensor quantities,  $\det$  indicates the determinant, and the superscripts  $^{-1}$ ,  $^T$  and  $^{-T}$  denote the inverse, the transpose, and the inverse transpose, respectively. In spite of the different notation utilized, it can be shown that equations (3) and (4) can be reconciled with the results obtained via the covariant formulation [43].

It is readily observed from equations (4) and (5) that *real-valued* transformations inherently yield *real-valued* constitutive tensors, and hence *lossless* (and *gainless*) transformation media, whereas *complex-valued* transformations may instead induce the presence of loss and/or gain.

In [19], we focused on particular classes of complex-coordinate transformations that generate media featuring *balanced* loss and gain spatial distributions fulfilling the  $\mathcal{PT}$ -symmetry condition [27–29]. More specifically, by recasting the transformed Maxwell’s equation in a pseudo-Hamiltonian form, we showed that the scalar (quantum-mechanics or paraxial-optics)  $\mathcal{PT}$ -symmetry condition can be generalized to our vector scenario as follows

$$\vec{\varepsilon}(-\mathbf{r}) = \vec{\varepsilon}^*(\mathbf{r}), \quad \vec{\mu}(-\mathbf{r}) = \vec{\mu}^*(\mathbf{r}), \quad (6)$$

with  $*$  denoting complex conjugation. As for the scalar case [27–29], these represent necessary (but not sufficient) conditions for attaining a purely real eigenspectrum. Moreover, we showed that coordinate transformations characterized by

$$\vec{\Lambda}(-\mathbf{r}) = \vec{\Lambda}^*(\mathbf{r}) \quad (7)$$

automatically satisfy such conditions. Similar to the scalar case [27–29], the fulfillment of equation (7) guarantees that

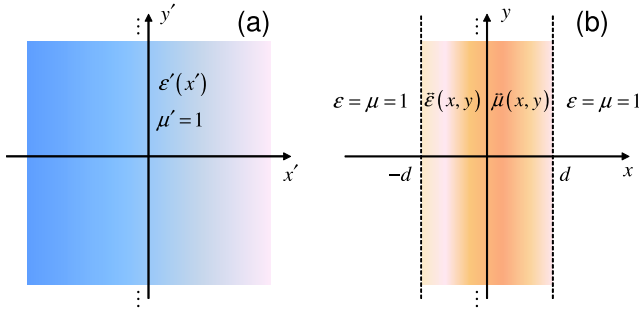


**Figure 1.** Problem schematic. (a) Auxiliary space, filled up with a nonmagnetic medium with generic relative permittivity distribution  $\epsilon'(x')$ . (b) Physical space containing the transformation slab, with constitutive tensors given by equation (9). Different color shadings are used to indicate regions that are generally inhomogeneous.

the eigenspectrum remains real as long as the ‘non-Hermiticity’ (gain/loss) level stays below a critical threshold. Above this threshold, an abrupt phase transition to a *complex* eigenspectrum (‘spontaneous  $\mathcal{PT}$ -symmetry breaking’) may typically occur. Remarkably, this phenomenon can be related to the (dis)continuity properties of the coordinate transformation [19]. More specifically, *continuous* coordinate transformations (1) (subject to equation (7)) from an auxiliary (lossless/gainless) space yield  $\mathcal{PT}$ -symmetric transformation media that do not undergo spontaneous symmetry breaking, whereas *discontinuous* transformations may generally induce this phenomenon.

As illustrative application examples, we considered continuous transformations that provide a  $\mathcal{PT}$ -symmetric metamaterial interpretation (and implementation) of a CSP, and discontinuous transformations that induce symmetry-breaking phenomena associated with *anisotropic transmission resonances*, such as ‘unidirectional invisibility’.

### 3. New results: Non-Hermitian transformation slabs

#### 3.1. Problem geometry and generalities

Referring to figure 1 for illustration, we consider a two-dimensional (2D) scenario, with  $z$ -invariant geometry and fields, and transverse-magnetic (TM) polarization (i.e.  $z$ -directed magnetic field). More specifically, we focus our attention on slab-type configurations, generated from an auxiliary space  $(x', y', z')$  filled up with a nonmagnetic medium with generic relative-permittivity distribution  $\epsilon'(x')$  (figure 1(a)). To this auxiliary configuration, we apply a general class of coordinate transformations

$$\begin{aligned} x' &= u(x), \\ y' &= v(x)y + w(x), \\ z' &= \alpha z, \end{aligned} \quad (8)$$

within the region  $|x| < d$ , with  $u$ ,  $v$  and  $w$  generally denoting complex-valued functions, and  $\alpha$  a complex-valued constant parameter. Applying the TO formalism, the associated field-manipulation capabilities can be equivalently obtained via a

‘transformation slab’ occupying the region  $|x| < d$  in the actual physical space  $(x, y, z)$  (figure 1(b)), with constitutive tensors (cf equation (4))

$$\frac{\vec{\epsilon}(x, y)}{\epsilon'(x')} = \vec{\mu}(x, y) = \begin{bmatrix} \frac{\alpha v}{\dot{u}} & -\frac{\alpha(\dot{v}y + \dot{w})}{\dot{u}} & 0 \\ -\frac{\alpha(\dot{v}y + \dot{w})}{\dot{u}} & \frac{\alpha[\dot{u}^2 + (\dot{v}y + \dot{w})^2]}{\dot{u}v} & 0 \\ 0 & 0 & \frac{\dot{u}v}{\alpha} \end{bmatrix}, \quad (9)$$

where the overdot denotes differentiation with respect to the argument, and the explicit  $x$ -dependence has been omitted for notational compactness. It is worth pointing out that the analytic mapping (3) is strictly valid in the presence of *continuous* transformations. In our case, assuming the exterior region  $|x| > d$  filled up with vacuum (cf figure 1(b)), this is ensured by the matching conditions

$$v(-d) = v(d) = \alpha = 1, \quad (10)$$

which imply that the transformations in equation (8) reduce to the identity at the interfaces  $x = \pm d$ , apart from irrelevant (possibly complex-valued) shifts along the  $x$ - and  $y$ -directions. Loosely speaking, this means that the reflection/transmission properties of the auxiliary space are preserved, apart from (possibly complex-valued) phase factors.

Moreover, we observe from equation (9) that, for the assumed TM polarization, the resulting transformation medium is *effectively nonmagnetic* (i.e.  $\mu_{zz} = 1$ ) provided that

$$v(x) = \frac{1}{\alpha \dot{u}(x)}. \quad (11)$$

Finally, we point out that the coordinate transformations in equation (8) are formally similar to (though slightly more general than) those previously considered by us in [44]. However, while the study [44] is restricted to real-valued transformations, here we allow the functions  $u$ ,  $v$ ,  $w$  and the parameter  $\alpha$  to be generally complex-valued, thereby exploring general classes of non-Hermitian transformation slabs.

One of the pivotal characteristics of conventional TO is its intuitive geometrical interpretation in terms of local distortion of the geodesic path of light rays, which essentially drives the conceptual design [33, 34]. One may argue that such an attractive feature is lost in our complex-coordinate extension. Nevertheless, in spite of the general complications, there are in fact instances of modeling tools and concepts in EM and optics that inherently rely on spatial and/or spectral quantities residing in a complex-coordinate space, and admit *remarkably simple* geometrical and physical interpretations. In what follows, we explore two notable cases.

#### 3.2. Complex-source-point-based beam manipulation

As the first application example, we consider the manipulation of CSP-based beams. The CSP formalism is a well-known and powerful tool in EM and optics for the modeling of beam-like excitations in configurations for which the solution pertaining to point-source illumination (Green’s

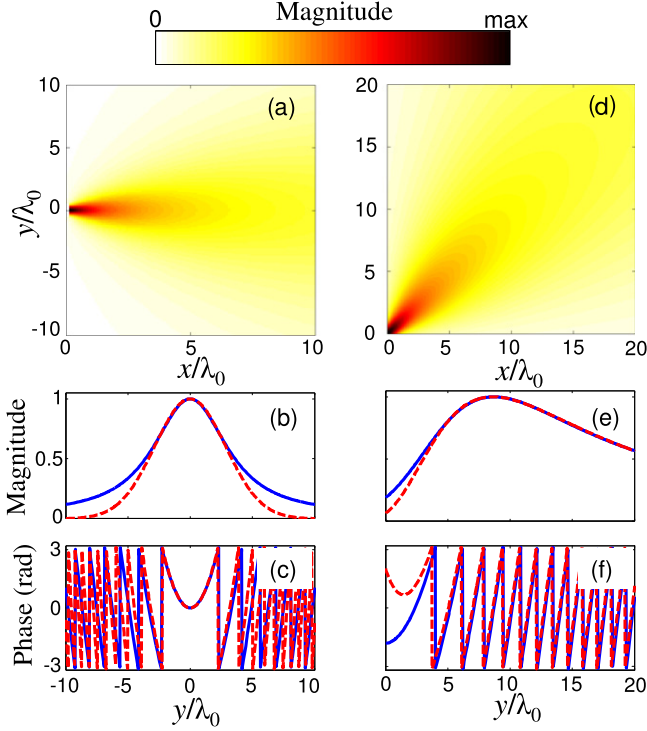


**Figure 2.** (a) Magnetic-field magnitude ( $|H_z|$ ) map pertaining to a CSP with  $x_s = y_s = 0$ ,  $b_s = \lambda_0/2$  and  $\theta_s = 0$  (cf equation (13)). (b), (c) Corresponding magnitude and phase cuts, respectively, at  $x = 5\lambda_0$  (blue-solid curves) compared with those pertaining to a conventional Gaussian beam with waist located at  $(x_s, y_s)$ , propagation axis forming an angle  $\theta_s$  with the  $x$ -axis, and Rayleigh parameter equal to  $b_s$  (red-dashed curves). (d)–(f) Same as panels (a)–(c), but for CSP parameters  $x_s = y_s = 0$ ,  $b_s = \lambda_0$  and  $\theta_s = \pi/4$ , and with linear cuts at  $x = 10\lambda_0$ . Field cuts are normalized with respect to the peak values.

function) is known analytically in exact or approximate forms [35, 36]. In our example, we start considering a unit-amplitude ( $V/m^2$ ),  $z$ -directed magnetic line-source,

$$M_z(x, y) = \delta(x - \tilde{x}_s)\delta(y - \tilde{y}_s), \quad (12)$$

radiating in vacuum. In equation (12),  $\delta$  denotes the Dirac-delta function, and

$$\tilde{x}_s = x_s + ib_s \cos \theta_s, \quad \tilde{y}_s = y_s + ib_s \sin \theta_s, \quad (13)$$

represents a complex-valued position, with  $x_s$ ,  $y_s$ ,  $b_s$  and  $\theta_s$  assumed as real-valued, and  $b_s > 0$ . Here and henceforth, complex-valued spatial quantities are identified by a tilde  $\sim$ . It can be shown [35, 36] (see also appendix A) that the corresponding radiated field (calculated via analytic continuation of a 2D Green's function) corresponds to a beam-like wave-object which, in the paraxial limit, is well approximated by a Gaussian beam [45] with waist located at  $(x_s, y_s)$ , propagation axis forming an angle  $\theta_s$  with the  $x$ -axis, and Rayleigh parameter equal to  $b_s$ . This is exemplified in figure 2, which shows two (magnitude) field maps for representative values of the CSP parameters, from which the beam-like behaviour is evident. Also shown are the magnitude and phase distributions along a linear cut, compared with those pertaining to the associated Gaussian

beam, from which the approximate equivalence can be observed in the paraxial region. Here, and henceforth,  $\lambda_0 = 2\pi c/\omega = 2\pi/k_0$  denotes the vacuum wavelength, with  $c$  and  $k_0$  being the corresponding wavespeed and wavenumber, respectively.

We now consider a CSP beam in the presence of our metamaterial transformation slab. In all examples below, we assume that the auxiliary space is entirely filled up by vacuum (i.e.  $\varepsilon'(x') = 1$  in figure 1(a)), the reflectionless conditions (10) hold, and the CSP beam waist is located outside the slab, say  $x_s \leq -d$ . Under these conditions, it can be shown (see appendix B for details) that the response at the other side of the slab ( $x \geq d$ ) can be effectively interpreted as generated by an ‘image’ CSP

$$\tilde{x}_i = x_i + ib_i \cos \theta_i, \quad \tilde{y}_i = y_i + ib_i \sin \theta_i, \quad (14)$$

which is related to the input CSP and transformation parameters via

$$\begin{aligned} \tilde{x}_i &= \tilde{x}_s + 2d - u(d) + u(-d), \\ \tilde{y}_i &= \tilde{y}_s - w(d) + w(-d). \end{aligned} \quad (15)$$

Equation (15) describes in a remarkably simple and physically-incisive fashion the image-formation properties of our transformation slab, via direct CSP-mapping between the input and output beams. Within this framework, a few considerations and remarks are in order. First, we observe that the results in equation (15) depend only on the boundary values of the mapping functions, and not on their actual behaviour in the slab region; this potentially leaves useful degrees of freedom in the design. Moreover, *real-valued* transformations can only affect the CSP real part, which, in physical terms, translates into the manipulation of the beam waist location. This is consistent with the typical manipulations (e.g. beam shifting, perfect radome, etc) explored in [44] without resorting to the CSP formalism. Conversely, the complex-coordinate TO extension proposed here can manipulate the imaginary part too, thereby enabling for *full* control of the CSP beam parameters, including the propagation direction and Rayleigh parameter. In what follows, we illustrate some representative examples.

A first interesting case is given by the condition

$$u(d) = u(-d), \quad w(-d) = w(d), \quad (16)$$

which, from equation (15), yields

$$\tilde{x}_i = \tilde{x}_s + 2d, \quad \tilde{y}_i = \tilde{y}_s. \quad (17)$$

In other words, the illuminating field generated by the input CSP at the interface  $x = -d$  is exactly reproduced at the output interface  $x = d$ , as if the slab were not present. The transformation slab therefore acts as an EM ‘nullity’. Working with real-valued coordinate transformations, such a condition for the function  $u$  can only be attained by enforcing a constant value (which would yield extreme-parameter transformation media) or a non-monotonic behaviour (which would correspond to a combination of complementary materials with positive and negative parameter values, similar to those studied in [46]). Within this framework, complex-



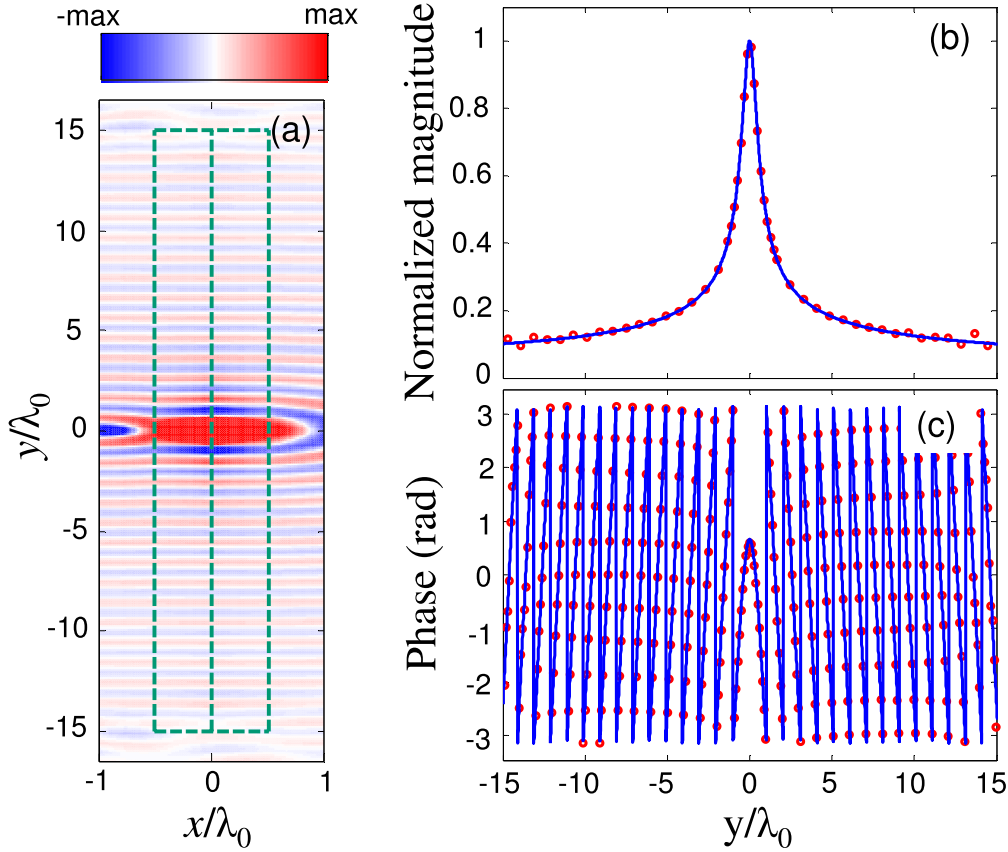


**Figure 3.** (a) Finite-element-computed magnetic-field ( $H_z$ ) real-part map pertaining to the  $\mathcal{PT}$ -symmetric transformation bi-layer in equation (19), with  $d = 0.5\lambda_0$ ,  $\chi = 0.3\lambda_0$  and finite aperture of  $30\lambda_0$ , excited by a CSP with  $x_s = -\lambda_0$ ,  $y_s = 0$ ,  $b_s = 0.1\lambda_0$ , and  $\theta_s = 0$ . The corresponding material parameters (cf equation (19)) are  $\varepsilon_{xx} = \mp i5/3$  and  $\varepsilon_{yy} = \mu_{zz} = \pm i3/5$  for  $-d < x < 0$  and  $0 < x < d$ , respectively. (b) Magnitude and (c) phase distributions (red dots) computed at the interface  $x = d + \lambda_0/100$ , compared with the theoretical predictions (blue-solid curves) in terms of an image CSP with  $x_i = x_s + 2d$ ,  $y_i = y_s$ ,  $b_i = b_s$ ,  $\theta_i = \theta_s$  (cf equation (17)). Results are normalized with respect to the theoretical solution evaluated at  $x = d + \lambda_0/100$  and  $y = 0$ . The dashed contour delimits the bi-layer region.

coordinate transformations provide more flexibility and additional degrees of freedom. For instance, considering the following transformation

$$u(x) = i\chi \left(1 - \frac{|x|}{d}\right), \quad v(x) = 1, \quad w(x) = 0, \quad (18)$$

with  $\chi$  denoting a real positive constant, we obtain a piecewise-homogeneous bi-layer with uniaxial media characterized by a balanced spatial distribution of gain and loss in the relevant constitutive-tensor components,

$$\varepsilon_{xx}(x) = \text{sgn}(x) \frac{id}{\chi}, \quad \varepsilon_{yy}(x) = \mu_{zz}(x) = -\text{sgn}(x) \frac{i\chi}{d}, \quad (19)$$

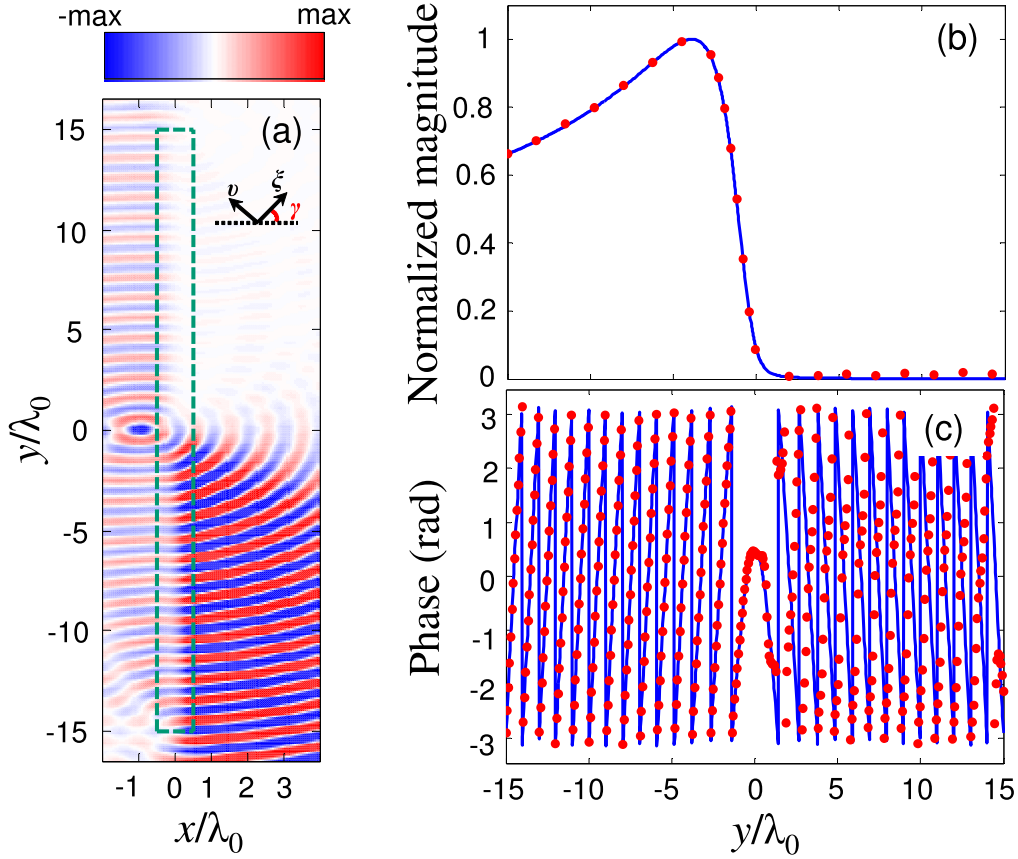
which fulfills the  $\mathcal{PT}$ -symmetry condition (6) (with  $\text{sgn}$  denoting the signum function). Such transformation medium was also considered in [19] within a different context, and a possible multilayered implementation was explored. Similar uniaxial media, simultaneously featuring gain and loss along different directions, have also been recently studied in [47].

Figure 3 shows the response of such an EM ‘nullity’ metamaterial transformation slab (with  $d = 0.5\lambda_0$ , transverse aperture of  $30\lambda_0$ , and  $\chi = 0.3\lambda_0$ ) due to a CSP beam with waist located at  $(x_s = -\lambda_0, y_s = 0)$  and diffraction length  $b_s = 0.1\lambda_0$ ,

impinging along the positive  $x$ -direction ( $\theta_s = 0$ ). More specifically, figure 3(a) shows the finite-element-computed (see appendix C for details) magnetic-field (real-part) map, from which it is rather evident that the impinging wavefront at the input slab interface  $x = -d$  is reproduced at its output ( $x = d$ ). For a more quantitative assessment, figures 3(b) and (c) compare the magnitude and phase field distributions, respectively, at the slab output with the theoretical prediction in equation (17) for an infinite slab. The agreement is very good, with the small oscillations towards the ends of the slab aperture attributable to truncation effects.

It is worth stressing that in the above example (as well as the following ones) the parameter configuration was chosen for a simple and direct illustration of the phenomenon, while maintaining a moderately-sized computational domain. At this stage, no particular attempt was made to optimize the geometry and material parameters in order to ensure the technological feasibility. For instance, the magnetic character in equation (19) may be traded off (via equation (11)) with a more complex (inhomogeneous, and with spatially-variant optical axis) spatial distribution.

In the above example, the manipulation was restricted to the CSP waist location, and therefore it could have been



**Figure 4.** (a) Finite-element-computed magnetic-field ( $H_z$ ) real-part map pertaining to the transformation slab in equation (20), with  $u_0 = 1.118$ ,  $|w_0| = 0.5$ ,  $\psi = \pi/2$ ,  $d = 0.5\lambda_0$  and finite aperture of  $30\lambda_0$ , excited by a real (i.e.  $b_s = 0$ ) line-source located at  $x_s = -\lambda_0$ ,  $y_s = 0$ . (b) Magnitude and (c) phase distributions (red dots) computed at the interface  $x = d + \lambda_0/100$ , compared with the theoretical predictions (blue-solid curves) in terms of an image CSP with  $x_i = -1.118\lambda_0$ ,  $y_i = 0$ ,  $b_i = 0.5\lambda_0$ ,  $\theta_i = -\pi/2$  (cf equation (15)). Results are normalized with respect to the theoretical solution evaluated at  $x = d + \lambda_0/100$  and  $y = -3.875\lambda_0$ . The dashed contour delimits the slab region. Also shown in panel (a) is the principal reference system ( $\xi$ ,  $v$ ), rotated by an angle  $\gamma = \pi/4$ , in which the transformation medium assumes a *uniaxial* form, with relevant components  $\varepsilon_{\xi\xi} = 0.894 - i0.447$ ,  $\varepsilon_{vv} = 0.894 + i0.447$ ,  $\mu_{zz} = 1.118$ .

achieved as well via real-valued coordinate transformations. We now consider a different class of transformations that can enable more general manipulations. In particular, we focus on the possibly simplest form

$$u(x) = u_0x, \quad v(x) = 1, \quad w(x) = w_0x, \quad \alpha = 1, \quad (20)$$

with  $u_0$  and  $w_0$  denoting complex-valued constant parameters represented in polar form as

$$u_0 = |u_0| \exp(i\phi), \quad w_0 = |w_0| \exp(i\psi). \quad (21)$$

Such transformations satisfy the matching conditions in equation (10) and, as it can be observed from equation (15), they affect *both* the real (via  $u_0$ ) and imaginary (via  $w_0$ ) parts of the CSP. The resulting transformation medium (cf (9)), with  $\mu_{zz} = u_0$  and

$$\vec{\varepsilon} = \begin{bmatrix} \frac{1}{u_0} & -\frac{w_0}{u_0} & 0 \\ -\frac{w_0}{u_0} & u_0 \left(1 + \frac{w_0^2}{u_0^2}\right) & 0 \\ 0 & 0 & u_0 \end{bmatrix}, \quad (22)$$

is homogeneous and generally anisotropic. However, conditions can be derived on transformations (20) so that the anisotropy reduces to a simpler *uniaxial* form (with tilted optical axis). As detailed in appendix D, such a condition can be expressed in a simple analytical form,

$$|u_0| = \sqrt{\frac{(1 + |w_0|^2) \sin \psi}{\sin(\psi - 2\phi)}}, \quad (23)$$

which admits feasible solutions provided that

$$\frac{\sin \psi}{\sin(\psi - 2\phi)} > 0. \quad (24)$$

We observe, for instance, that for real-valued  $w_0$  (i.e.  $\psi = \pm n\pi$ ,  $n \in \mathbb{N}$ ), the only feasible ( $u_0 \neq 0$ ) solution of equation (23) implies  $\phi = \pm(n + 1/2)\pi$ ,  $n \in \mathbb{N}$ , i.e. either real or purely imaginary  $u_0$ .

As a first example, figure 4 shows the response of a slab designed so as to ‘transform’ a conventional line-source ( $x_s = -\lambda_0$ ,  $y_s = 0$ ,  $b_s = 0$ ) into an image CSP representing a beam propagating along the negative  $y$ -direction ( $x_i = -1.118\lambda_0$ ,  $y_i = 0$ ,  $b_i = 0.5\lambda_0$ ,  $\theta_i = -\pi/2$ ). Parameters

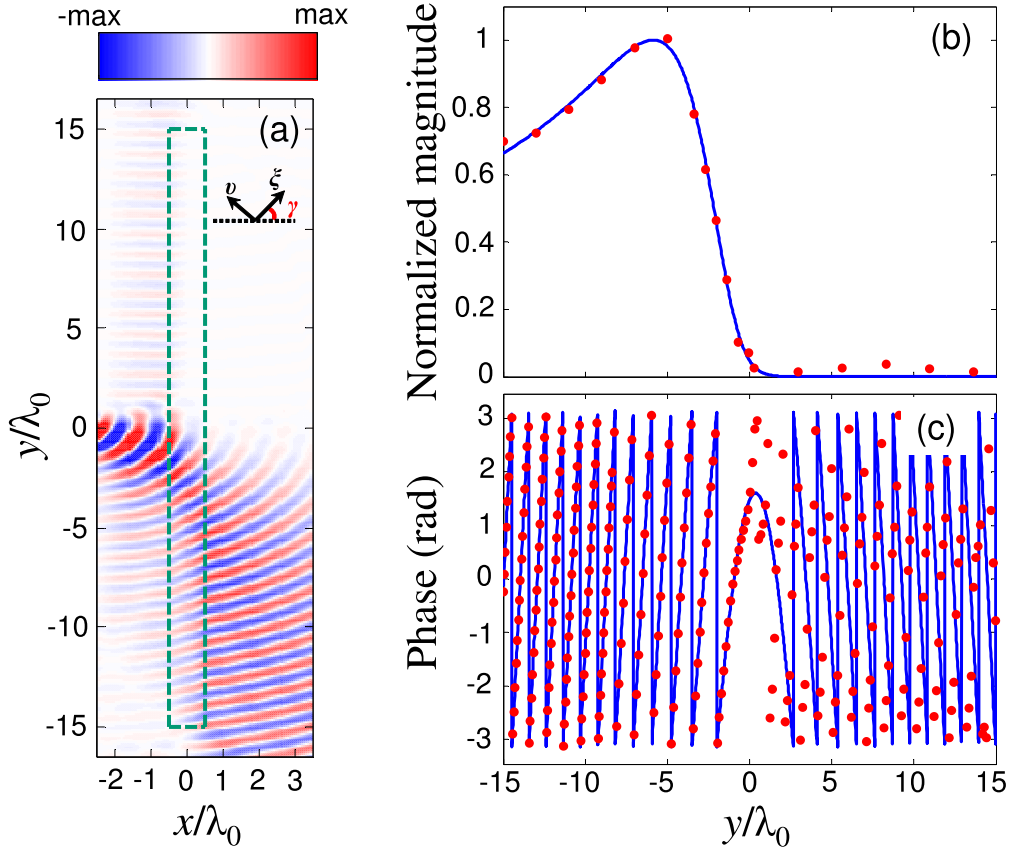


**Figure 5.** (a) Finite-element-computed magnetic-field ( $H_z$ ) real-part map pertaining to the transformation slab in equation (20), with  $|u_0| = 1.085$ ,  $\phi = -0.150\pi$ ,  $|w_0| = 0.5$ ,  $\psi = \pi/3$ ,  $d = 0.5\lambda_0$  and finite aperture of  $30\lambda_0$ , excited by a CSP with  $x_s = -3\lambda_0$ ,  $y_s = 0$ ,  $b_s = \lambda_0$ ,  $\theta_s = -\pi/6$ . (b) Magnitude and (c) phase distributions (red dots) computed at the interface  $x = d + \lambda_0/100$ , compared with the theoretical predictions (blue-solid curves) in terms of an image CSP with  $x_i = x_s$ ,  $y_i = 0.25\lambda_0$ ,  $b_i = b_s$ ,  $\theta_i = -0.379\pi$  (cf equation (15)). Results are normalized with respect to the theoretical solution evaluated at  $x = d + \lambda_0/100$  and  $y = -5.866\lambda_0$ . The dashed contour delimits the slab region. Also shown in panel (a) is the principal reference system ( $\xi$ ,  $\eta$ ), rotated by an angle  $\gamma = 0.137\pi$ , in which the transformation medium assumes a *uniaxial* form, with relevant components  $\varepsilon_{\xi\xi} = 0.829 - i0.628$ ,  $\varepsilon_{\eta\eta} = 0.766 + i0.581$ ,  $\mu_{zz} = 0.970 + i0.495$ .

are chosen so as to fulfill the conditions in equations (23) and (24), and hence the arising transformation medium reduces to a homogeneous, uniaxially-anisotropic material with a  $45^\circ$ -tilted optical axis, and components exhibiting both gain and loss along different directions. As it can be observed from the field-map (figure 4(a)), as well as the relevant magnitude (figure 4(b)) and phase (figure 4(c)) distributions, the isotropic radiation produced by the real line-source is converted by the slab in a markedly directional beam, in excellent agreement with the theoretical prediction.

Figure 5 shows a further example, where an obliquely-incident CSP beam with  $x_s = -3\lambda_0$ ,  $y_s = 0$ ,  $b_s = \lambda_0$ ,  $\theta_s = -\pi/6$  is converted into a beam represented by an image CSP with  $x_i = x_s$ ,  $y_i = 0.25\lambda_0$ ,  $b_i = b_s$ ,  $\theta_i = -0.379\pi$ , thereby producing a shift (along the  $y$ -direction) of the waist location and an angular steering of nearly  $40^\circ$ . Once again, the resulting transformation medium assumes a uniaxially-anisotropic form (with a  $\sim 25^\circ$ -tilted optical axis, and components exhibiting both gain and loss), and the agreement between numerical simulations and theoretical predictions is very good.

To sum up, the proposed classes of transformations allow, in principle, rather general manipulations of CSP-based beam-like wave objects. Clearly, suitable restrictions should be enforced in order to achieve structural simplifications such as uniaxial anisotropy, positive real-parts of the constitutive parameters, and feasible levels of gain. We highlight that, besides the possible applications to the design of active optical devices, such as lasers, lenses and imaging systems, the above framework also provides a simple and yet powerful geometrical interpretation of the complex-coordinate TO extension, with the CSP-based beam propagators playing the role of light rays in conventional TO. Within this framework, it is also worth mentioning that CSP-based beam propagators can be utilized as efficient basis functions to model general illuminating field distributions [48].

### 3.3. Leaky-wave manipulation

As a second illustrative application, we consider the manipulation of LWs, associated with *complex-valued* roots of the dispersion equations of open (e.g. dielectric) waveguides [49]. To this aim, we start considering an auxiliary space

containing a homogeneous, lossless slab of thickness  $2d$ , i.e.

$$\varepsilon'(x') = \begin{cases} \varepsilon_b, & |x'| < d, \\ 1, & |x'| > d, \end{cases} \quad (25)$$

with  $\varepsilon_b \neq 1$ , in figure 1(a). As is well known, this simple waveguiding structure can support *modal* (source-free) solutions that satisfy the dispersion equation [49]

$$\cot(2k'_{xb}d) = \frac{i\varepsilon_b k'_x}{2k'_{xb}} + \frac{ik'_{xb}}{2\varepsilon_b k'_x}, \quad (26)$$

where  $k'_y$  and  $k'_x = \sqrt{k_0^2 - k_y'^2}$  denote the spectral-domain wavenumbers associated to the  $y'$  and  $x'$  variables, respectively, and  $k'_{xb} = \sqrt{k_0^2 \varepsilon_b - k_y'^2}$ . The solutions of equation (26) are generally to be found in the *complex*  $k'_y$  plane. In view of the underlying symmetry, without loss of generality, we focus on the case  $\text{Re}(k'_y) > 0$  (i.e. propagation along the positive  $y'$  direction). In particular, *real-valued* solutions,

$$\text{Im}(k'_y) = 0, \quad k'_y > k_0, \quad \text{Im}(k'_x) \geq 0, \quad (27)$$

correspond to the well-known *guided* (or *bound*) modes that propagate without attenuation along the  $y'$ -direction, and decay exponentially along the  $x'$ -direction [49]. On the other hand, we can also identify a class of *complex-valued* solutions

$$\text{Re}(k'_y) < k_0, \quad \text{Im}(k'_y) \leq 0, \quad (28)$$

that are typically referred to as LW modes [49]. We stress that the complex-valued character of these roots is generally not related to the presence of loss/gain; in fact, these solutions may also be found in the lossless (and gainless) scenario considered here. These LW solutions belong to the so-called ‘improper’ spectrum, as they grow exponentially along the  $x'$ -direction, thereby violating the radiation condition [49]. Though not directly observable in the far field, LW modes can be utilized to represent the field distribution nearby the slab aperture. Such LW-based modeling can effectively capture the radiation properties of the slab, and its use is widespread in the EM and antenna communities [50]. In essence, assuming that a LW with complex propagation constant  $k'_{ys} = \pm(\beta + i\eta)$  is the dominant mode excited (via proper illumination), the field radiated by the slab can be approximated as generated by an equivalent aperture field distribution [50]

$$H_z^{(eq)}(y') \sim \exp(i\beta |y'|) \exp(-\eta |y'|), \quad (29)$$

which, in the far region, yields the radiation pattern [50]

$$|H_z^{(eq)}(\theta')|^2 \sim \cos^2 \theta' \left\{ \frac{\beta^2 + \eta^2}{[k_0^2 \sin^2 \theta' - (\beta^2 - \eta^2)]^2 + (2\beta\eta)^2} \right\}, \quad (30)$$

with  $\theta'$  denoting the radiation angle measured from the  $x'$ -axis. Therefore, also in this case, the real and imaginary parts of the LW propagation constant admit a simple and insightful physical interpretation that is tied with the main radiation characteristics (direction and beamwidth). It appears therefore suggestive to explore to what extent our complex-coordinate TO extension can manipulate these quantities so that, given

an LW solution supported by the dielectric slab in the auxiliary domain, one may design a metamaterial transformation slab that supports (among others) an LW with a suitably modified propagation constant. To this aim, we consider the possibly simplest class of transformations

$$u(x) = u_0 x, \quad v(x) = v_0, \quad w(x) = 0, \quad \alpha = u_0 v_0, \quad (31)$$

with  $u_0$  and  $v_0$  denoting complex-valued constant parameters. Such simple transformations essentially constitute a complex coordinate scaling. However, unlike the previous examples, they do not satisfy (apart from the trivial case  $u_0 = v_0 = 1$ ) the matching conditions in equation (10), while they do fulfill the condition in equation (11) for an effectively nonmagnetic character. Although the dispersion equation in the transformed domain cannot be obtained via direct mapping of equation (26), it can still be readily derived by following the standard procedure [49] and taking into account the coordinate scaling (31). We obtain

$$\cot(2k_{xb}u_0d) = \frac{i\varepsilon_b u_0 k_x}{2k_{xb}} + \frac{ik_{xb}}{2\varepsilon_b u_0 k_x}, \quad (32)$$

with  $k_y$  and  $k_x = \sqrt{k_0^2 - k_y^2}$  denoting the spectral-domain wavenumbers associated to the  $y$ - and  $x$ - variables, respectively, and  $k_{xb} = \sqrt{k_0^2 \varepsilon_b - k_y^2}$ . Assuming that the slab in the auxiliary domain supports a LW with propagation constant  $k'_{ys}$ , a sufficient condition for the transformed slab to support a LW with modified propagation constant  $k_{ys}$  can be obtained by equating the left- and right-hand sides of the dispersion equations (26) and (32) evaluated for  $k'_y = k'_{ys}$  and  $k_y = k_{ys}$ , respectively. Accordingly, by equating the right-hand sides, we obtain a bi-quadratic equation which directly yields

$$v_0 = \begin{cases} \pm \frac{k_{ys}}{\sqrt{\varepsilon_b(k_0^2 - \varepsilon_b k_{xs}' k_{xs})}}, \\ \pm \frac{k_{ys} \sqrt{k_{xs}'}}{\sqrt{\varepsilon_b k_0^2 (k_{xs}' - k_{xs}) + k_{xs} k_{ys}'^2}}, \end{cases} \quad (33)$$

with  $k_{xs} = \sqrt{k_0^2 - k_{ys}^2}$  and  $k_{xs}' = \sqrt{k_0^2 - k_{ys}'^2}$ . Then, by equating the cotangent arguments (thereby disregarding multiplicities), we get a simple algebraic equation that can be solved with respect to  $u_0$ , yielding

$$u_0 = \sqrt{\frac{k_0^2 \varepsilon_b - k_{ys}'^2}{k_0^2 \varepsilon_b - \frac{k_{ys}^2}{v_0^2}}}. \quad (34)$$

Equations (33) and (34) above enable for the desired mapping between the LW propagation constants  $k'_{ys}$  and  $k_{ys}$  in the two domains. It is worth pointing out that the above transformation is not restricted to the LW solution  $k'_{ys}$  of specific interest, but it rather affects the *entire* eigenspectrum of the slab in the auxiliary domain. Therefore, care should be taken to make sure that the transformed LW is actually the dominant mode.

A representative example is illustrated in figure 6. We start from a slab in the auxiliary domain with  $d = 0.125\lambda_0$  and  $\varepsilon_b = 0.05$ , which supports a LW mode with propagation



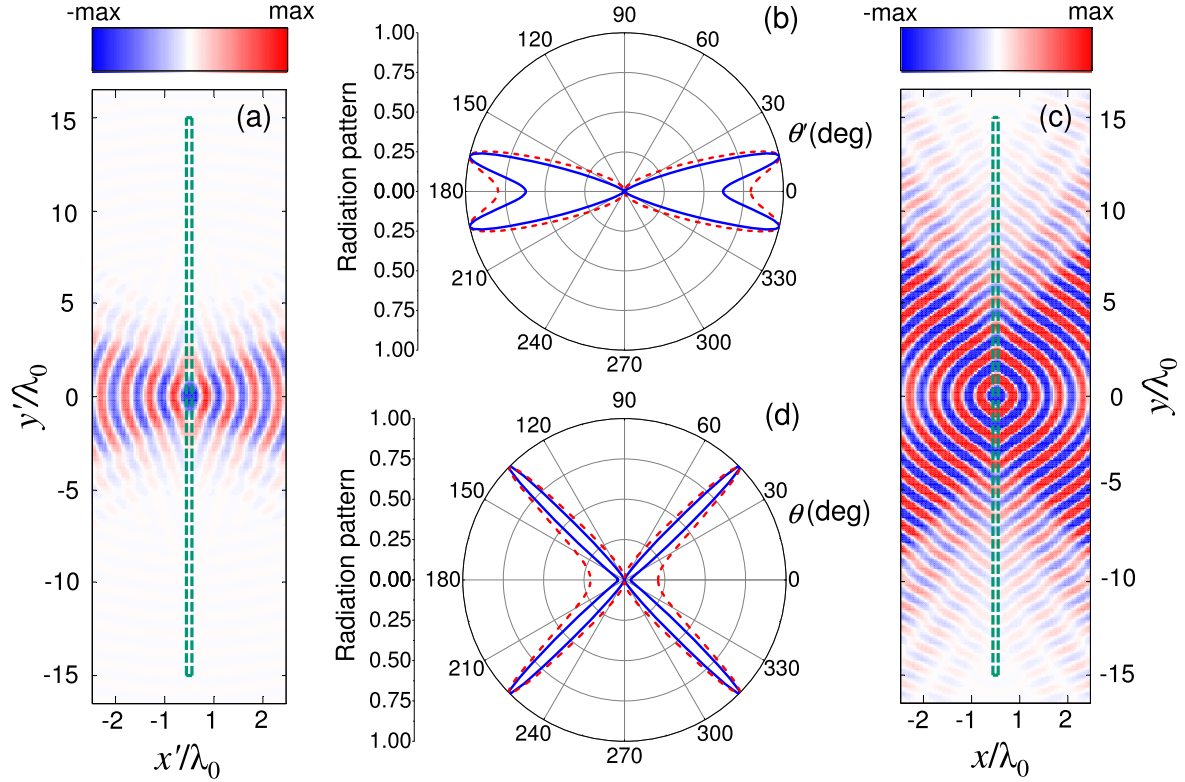


**Figure 6.** (a) Finite-element-computed magnetic-field ( $H_z$ ) real-part map pertaining to a slab in the auxiliary domain with  $\varepsilon_b = 0.05$ ,  $d = 0.125\lambda_0$  and finite aperture of  $30\lambda_0$ , excited by a magnetic line source located at  $x' = y' = 0$ . (b) Corresponding radiation pattern (red-dashed curve) compared with theoretical LW prediction (blue-solid curve) in (30), with  $k'_{ys} = \pm(0.257 + i0.120)k_0$ . (c), (d) Same as panels (a) and (b), respectively, but pertaining to a homogeneous, uniaxial transformation slab (cf (31), with  $u_0 = 1.170 + i0.0212$  and  $v_0 = 2.582 - i0.756$ ) with  $\varepsilon_{xx} = 0.305 - i0.195$ ,  $\varepsilon_{yy} = 0.068 + i0.003$ ,  $\mu_{zz} = 1$ , which supports a LW with  $k_{ys} = \pm(0.707 + i0.05)k_0$ .

constant  $k'_{ys} = \pm(0.257 + i0.120)k_0$ . Figure 6(a) shows the finite-element-computed (see appendix C for details) field-map pertaining to a line-source excitation located at  $x = y = 0$ , from which we can observe the radiated field accompanied by an exponentially-decaying (along the  $y$ -direction) behaviour of the field inside and nearby the slab, in accord with the LW-based modeling in equation (29). This is quantitatively more evident in figure 6(b), which compares the numerically computed far-field radiation pattern with the LW-based theoretical prediction in (30). The fairly good agreement is indicative of the dominant character of the LW mode. We now apply the coordinate transformations in equation (31) (with (33) and (34)), with the aim of designing a metamaterial transformation slab that supports an LW with a modified propagation constant  $k_{ys} = (0.707 + i0.05)k_0$ , so as to steer the beam direction to  $\theta = \pi/4$  and achieve a significantly smaller beamwidth (i.e. higher directivity). Accordingly, from our design equations (33) and (34), we obtain  $u_0 = 1.170 + i0.0212$  and  $v_0 = 2.582 - i0.756$ . Figures 6(c) and (d) show the field map and radiation pattern, respectively, pertaining to the corresponding transformation slab (with parameters in the caption) excited by the same line source. As it can be observed, the desired radiation characteristics are obtained, in fairly good agreement with the theoretical predictions.

By comparison with conventional TO-based approaches for tailoring the waveguiding [51, 52] and radiation [53–55]

properties, which rely on real-valued coordinate transformation to suitably shape the wavefronts or effectively scale the structure (so that, e.g., a small-sized antenna can exhibit radiation characteristics comparable with a larger one), our approach here manipulates directly the dispersion equation. The above results may pave the way to the development of new strategies for the design of active antennas, where the beam steering may be achieved (and actively controlled) via suitable modulation of loss and gain, rather than conventional phase shifters.

#### 4. Concluding remarks and perspectives

In summary, we have explored some general classes of non-Hermitian metamaterial slabs inspired by complex-coordinate transformations. Analytical and numerical results from our prototype studies indicate that complex-coordinate extensions of TO can be naturally and fruitfully utilized in conjunction with powerful EM analytic tools and formalisms based on the ‘complexification’ of spatial and spectral quantities (the most prominent examples being CSP-based beams and LWs, respectively), as well as pervasive paradigms such as  $\mathcal{PT}$ -symmetry. In particular, we focused on the interesting manipulation effects enabled by transformation slabs which, in their simplest configurations, are made of piecewise homogeneous, uniaxial (possibly with tilted optical axis)

media with constitutive parameters featuring both loss and gain along different directions.

We expect that these results may provide useful insight into the EM wave interactions with non-Hermitian scenarios, and may indicate new avenues in the design of active optical devices and radiating systems, where the use of gain is not limited to attain loss compensation. Within this framework, current and future research is aimed at extending the class of possible transformations and manipulations (also to 3D scenarios as well and cylindrical and spherical configurations). Also of interest is the optimization of the parameter configurations in order to address their practical implementation with feasible material constituents.

## Appendix A. Essentials on CSP modeling

Without loss of generality, we consider in equation (13) the case  $x_s = y_s = 0$  and  $\theta_s = 0$ , i.e.

$$\tilde{x}_s = ib_s, \quad \tilde{y}_s = 0, \quad (\text{A.1})$$

to which any arbitrary case can be reduced via suitable coordinate shifts and rotations. The *exact* solution of Maxwell's equations pertaining to the line-source (12) radiating in vacuum can be derived in closed form via analytical continuation of the well-known 2D Green's function [56], viz.,

$$\tilde{H}_z^{(s)}(x, y) = -\frac{\omega\varepsilon_0}{4}H_0^{(1)}(k_0\tilde{s}), \quad (\text{A.2})$$

where  $\varepsilon_0$  denotes the vacuum permittivity,  $H_0^1$  is the zeroth-order Hankel function of first kind [57], and

$$\tilde{s} = \sqrt{(x - ib_s)^2 + y^2} \quad (\text{A.3})$$

represents a complex distance. Two main choices can be made for the branch-cut in (A.3): either  $\text{Re}(\tilde{s}) \geq 0$  (generally referred to as the *source-type* solution) or  $\text{Im}(\tilde{s}) \leq 0$  (generally referred to as the *beam-type* solution) [36]. The source-type solution satisfies the radiation condition, and yields strong beam-like radiation in the halfspace  $x > 0$ , with only negligible radiation in the halfspace  $x < 0$ , which can be interpreted as generated by an equivalent source distribution occupying the region  $|y| < b_s$  in the real  $x = 0$  plane. Conversely, the beam-type solution can be interpreted as generated by equivalent sources located at  $x \rightarrow -\infty$ . Accordingly, it satisfies the radiation condition only for  $x > 0$ , and yields strong radiation both for  $x > 0$  and  $x < 0$ .

Considering the source-type solution  $\text{Re}(\tilde{s}) \geq 0$ , near the  $x$ -axis, the complex distance in (A.3) can be approximated as

$$\tilde{s} \approx \pm \left[ x - ib_s + \frac{y^2}{2(x - ib_s)} \right], \quad x \gtrless 0. \quad (\text{A.4})$$

By substituting (A.4) in (A.2), and exploiting the large-argument asymptotic approximation of the Hankel function

[57], we obtain

$$\begin{aligned} \tilde{H}_z^{(s)}(x, y) &\sim \frac{\Xi}{\sqrt{x - ib_s}} \\ &\times \exp \left[ \pm ik_0(x - ib_s) \pm i \frac{k_0 y^2}{2K(x)} \mp \frac{y^2}{W^2(x)} \right], \quad x \gtrless 0, \end{aligned} \quad (\text{A.5})$$

where  $\Xi$  is an irrelevant constant, and  $W$  and  $K$  denote the conventional spot-size and radius of curvature, respectively, of a Gaussian beam [45],

$$W(x) = W(0) \sqrt{1 + \left( \frac{x}{b_s} \right)^2}, \quad W(0) = \sqrt{\frac{2b_s}{k_0}}, \quad (\text{A.6})$$

$$K(x) = x + \frac{b_s^2}{x}. \quad (\text{A.7})$$

From the expression (A.5), it is evident that in the half-space  $x > 0$  and within the paraxial range, the exact CSP-based solution in equation (A.2) approximately matches a standard Gaussian beam with Rayleigh distance

$$x_R \equiv \frac{k_0 W^2(0)}{2} = b_s. \quad (\text{A.8})$$

On the other hand, it is also evident from equation (A.5) that the radiated field in the halfspace  $x < 0$  is much weaker (by a factor  $\exp(-k_0 b_s)$ ) and different from a Gaussian beam.

Similar approximations (not shown here for brevity) can be derived for the beam-type solution  $\text{Im}(\tilde{s}) \leq 0$ . In this case, one finds strong radiation and approximate equivalence with a Gaussian beam in both halfspaces.

In all our examples (figures 3–5), we have considered the source-type solution for both the illuminating and image CSPs. However, should the waist of the image CSP be located beyond the slab ( $x_i > d$ ), the beam-type solution would be the proper choice in order to correctly model the field within the region  $d < x < x_i$ .

## Appendix B. Details on the CSP mapping (15)

The derivation of the CSP mapping in (15) can be most easily understood in terms of analytic continuation of a configuration involving conventional (i.e. real-valued) line sources and real-valued coordinate transformations. To this aim, let us start considering the case of a conventional line-source located at  $x = x_s$  and  $y = y_s$ , whose radiated field (in the absence of the slab) is given by the well-known 2D Green's function [56],

$$\begin{aligned} H_z^{(s)}(x, y) &= -\frac{\omega\varepsilon_0}{4}H_0^{(1)}[k_0\sqrt{(x - x_s)^2 + (y - y_s)^2}] \\ &= -\frac{\omega\varepsilon_0}{4\pi} \int_{-\infty}^{\infty} \frac{1}{k_x} \exp \{ i[k_x |x - x_s| \\ &\quad + k_y(y - y_s)] \} dk_y, \end{aligned} \quad (\text{B.1})$$

with the second equality derived from the spectral–integral representation of the Hankel function [56], and  $k_x = \sqrt{k_0^2 - k_y^2}$ ,  $\text{Im}(k_x) \geq 0$ . Via straightforward plane-wave algebra, the field transmitted in the region  $x > d$  in the presence of the transformation slab can be written as

$$H_z^{(i)}(x, y) = \frac{1}{2\pi} \int_{-\infty}^{\infty} \hat{H}_z^{(s)}(k_x, k_y) T(k_x, k_y) \times \exp[i(k_x x + k_y y)] dk_y, \quad (\text{B.2})$$

where  $\hat{H}_z^{(s)}$  is the spatial Fourier transform of the incident field in equation (B.1), viz.,

$$\begin{aligned} \hat{H}_z^{(s)}(k_x, k_y) &= \int_{-\infty}^{\infty} H_z^{(s)}(x, y) \exp[-i(k_x x + k_y y)] dy \\ &= -\frac{\omega \varepsilon_0}{2k_x} \exp[-i(k_x x_s + k_y y_s)], \end{aligned} \quad (\text{B.3})$$

whereas  $T$  denotes the plane-wave transmission coefficient of the transformation slab. Assuming, for now, *real-valued* coordinate transformations, in view of the matching conditions in equation (10), the transmission coefficient can be derived by solving the straightforward problem in the auxiliary space (plane-wave propagation in vacuum) and subsequently mapping it in the actual physical space. Accordingly, we obtain a unit-magnitude transmission coefficient which essentially accounts for the phase accumulation through the (reflectionless) slab, viz.,

$$T(k_x, k_y) = \exp\{ik_x[u(d) - u(-d)] + ik_y[w(d) - w(-d)]\}. \quad (\text{B.4})$$

By substituting equations (B.3) and (B.4) in the spectral integral (B.2), we finally obtain

$$\begin{aligned} H_z^{(i)}(x, y) &= -\frac{\omega \varepsilon_0}{4\pi} \int_{-\infty}^{\infty} \frac{1}{k_x} \exp\{i[k_x |x - x_i| + k_y(y - y_i)]\} dk_y \\ &= -\frac{\omega \varepsilon_0}{4} H_0^{(1)}[k_0 \sqrt{(x - x_i)^2 + (y - y_i)^2}], \end{aligned} \quad (\text{B.5})$$

where the absolute value stems from the branch-cut choice for  $k_x$ , and we have defined the real-valued image coordinates

$$\begin{aligned} x_i &\equiv x_s + u(-d) - u(d) + 2d, \\ y_i &\equiv y_s + w(-d) - w(d). \end{aligned} \quad (\text{B.6})$$

The CSP mapping in equation (15) can be finally obtained as the analytic continuation of equations (B.5) and (B.6), by

considering complex-valued source coordinates  $(\tilde{x}_s, \tilde{y}_s)$  as well as complex-valued mapping functions  $u$  and  $w$ .

## Appendix C. Details on numerical simulations

For our full-wave numerical validations (figures 3–6), we utilized the finite-element-based commercial software package COMSOL Multiphysics (RF module) [58]. For the examples in figures 3 and 5, the excitation was defined (at the left boundary of the computational domain) as a magnetic-field distribution given by the CSP model in equation (A.2); the remaining three boundaries of the computational domain were terminated by a wavelength-thick perfectly-matched layer (PML). For the examples in figures 4 and 6, a magnetic line-source was instead utilized, with PML terminations at all four boundaries of the computational domain. The far-field radiation patterns in figures 6(b) and (d) were obtained using a dedicated post-processing tool available in the RF module. In all examples, we utilized the MUMPS frequency-domain direct solver, and a triangular mesh with adaptive element size (ranging from  $\lambda_0/60$  to  $\lambda_0/20$ ), resulting into a number of degrees of freedom ranging from three to five million.

## Appendix D. Details on the uniaxiality condition (23)

In order to derive the condition in equation (23), we observe that the tensor in equation (22) can be diagonalized in the principal reference  $(\xi, v, z)$  constituted by its orthogonal eigenvectors. However, in view of the generally complex-valued nature of its components, the eigenvectors are also generally complex-valued, and hence the diagonal form does not necessarily admit a physical interpretation in terms of a uniaxial medium with a tilted optical axis. In order to derive the conditions under which such physical interpretation is valid, we start expressing in Cartesian  $(x, y, z)$  form the tensor pertaining to a medium that is uniaxial in a rotated (by an angle  $\gamma$  in the  $x$ – $y$  plane) orthogonal reference system  $(\xi, v, z)$ ,

$$\begin{bmatrix} \frac{1}{2}[\varepsilon_{\xi\xi} + \varepsilon_{vv} + (\varepsilon_{\xi\xi} - \varepsilon_{vv})\cos(2\gamma)] & (\varepsilon_{\xi\xi} - \varepsilon_{vv})\sin\gamma\cos\gamma & 0 \\ (\varepsilon_{\xi\xi} - \varepsilon_{vv})\sin\gamma\cos\gamma & \frac{1}{2}[\varepsilon_{\xi\xi} + \varepsilon_{vv} + (\varepsilon_{vv} - \varepsilon_{\xi\xi})\cos(2\gamma)] & 0 \\ 0 & 0 & 1 \end{bmatrix}, \quad (\text{D.1})$$

with  $\varepsilon_{\xi\xi}$  and  $\varepsilon_{vv}$  denoting the relevant components (eigenvalues) along the principal axes  $\xi$  and  $v$ , respectively. The sought condition can be derived by equating component-wise the above tensor with equation (22), solving with respect to  $\varepsilon_{\xi\xi}$ ,  $\varepsilon_{vv}$  and  $\gamma$ , and enforcing real values of  $\gamma$ . By equating the diagonal terms, we obtain two linear

equations in  $\varepsilon_{\xi\xi}$  and  $\varepsilon_{vv}$ , which yield

$$\varepsilon_{\xi\xi} = \frac{1}{2u_0} [1 + u_0^2 + w_0^2 - \sec(2\gamma)(u_0^2 + w_0^2 - 1)], \quad (\text{D.2})$$

$$\varepsilon_{vv} = \frac{1}{2u_0} [1 + u_0^2 + w_0^2 + \sec(2\gamma)(u_0^2 + w_0^2 - 1)]. \quad (\text{D.3})$$

Finally, by equating the off-diagonal terms, and substituting the above solutions, we obtain

$$\tan(2\gamma) = \frac{2w_0}{u_0^2 + w_0^2 - 1}. \quad (\text{D.4})$$

By assuming  $w_0 \neq 0$  (otherwise the uniaxial condition is trivially satisfied), and multiplying by  $w_0^*$  both the numerator and denominator of the right-hand side of equation (D.4), it readily follows that the rotation angle  $\gamma$  is real if

$$\text{Im}[w_0^*(u_0^2 + w_0^2 - 1)] = 0, \quad (\text{D.5})$$

from which the condition in equation (23) is straightforwardly obtained by substituting the polar representations in equation (21).

## References

- [1] Xiao S, Drachev V P, Kildishev A V, Ni X, Chettiar U K, Yuan H K and Shalaev V M 2010 *Nature* **466** 735–8
- [2] Makris K G, El-Ganainy R, Christodoulides D N and Musslimani Z H 2008 *Phys. Rev. Lett.* **100** 103904
- [3] Mostafazadeh A 2009 *Phys. Rev. Lett.* **102** 220402
- [4] Ruter C E, Makris K G, El-Ganainy R, Christodoulides D N, Segev M and Kip D 2010 *Nat. Phys.* **192**
- [5] Lin Z, Ramezani H, Eichelkraut T, Kottos T, Cao H and Christodoulides D N 2011 *Phys. Rev. Lett.* **106** 213901
- [6] Regensburger A, Bersch C, Miri M A, Onishchukov G, Christodoulides D N and Peschel U 2012 *Nature* **488** 167–71
- [7] Longhi S 2010 *Phys. Rev. A* **82** 031801
- [8] Chong Y D, Ge L and Stone A D 2011 *Phys. Rev. Lett.* **106** 093902
- [9] Fleury R, Sounas D L and Alù A 2014 *Phys. Rev. Lett.* **113** 023903
- [10] Longhi S 2014 *Opt. Lett.* **39** 1697–700
- [11] Kulishov M, Kress B and Slavík R 2013 *Opt. Express* **21** 9473
- [12] Peng B, Özdemir Ş K, Lei F, Monifi F, Gianfreda M, Long G L, Fan S, Nori F, Bender C M and Yang L 2014 *Nat. Phys.* **10** 394–8
- [13] Feng L, Wong Z J, Ma R, Wang Y and Zhang X 2014 arXiv:1405.2863
- [14] Principe M, Castaldi G, Consales M, Cusano A and Galdi V 2015 *Sci. Rep.* **5** 8568
- [15] Benisty H, Degiron A, Lupu A, De Lustrac A, Chénais S, Forget S, Besbes M, Barbillon G, Bruyant A, Blaize S and Lérondel G 2011 *Opt. Express* **19** 18004–19
- [16] Nazari F, Bender N, Ramezani H, Moravvej-Farshi M, Christodoulides D N and Kottos T 2014 *Opt. Express* **22** 9574–84
- [17] Zhu X, Feng L, Zhang P, Yin X and Zhang X 2013 *Opt. Lett.* **38** 2821
- [18] Sounas D L, Fleury R and Alù A 2015 *Phys. Rev. Appl.* **4** 014005
- [19] Castaldi G, Savoia S, Galdi V, Alù A and Engheta N 2013 *Phys. Rev. Lett.* **110** 173901
- [20] Alaeian H and Dionne J A 2014 *Phys. Rev. A* **89** 033829
- [21] Alaeian H and Dionne J A 2014 *Phys. Rev. B* **89** 075136
- [22] Savoia S, Castaldi G, Galdi V, Alù A and Engheta N 2014 *Phys. Rev. B* **89** 085105
- [23] Savoia S, Castaldi G, Galdi V, Alù A and Engheta N 2015 *Phys. Rev. B* **91** 115114
- [24] Gear J, Liu F, Chu S T, Rotter S and Li J 2015 *Phys. Rev. A* **91** 033825
- [25] Longhi S, Gatti D and Della Valle G 2015 *Sci. Rep.* **5** 13376
- [26] Poli C, Bellec M, Kuhl U, Mortessagne F and Schomerus H 2015 *Nat. Commun.* **6** 6710
- [27] Bender C M and Boettcher S 1998 *Phys. Rev. Lett.* **80** 5243–6
- [28] Bender C M, Brody D C and Jones H F 2002 *Phys. Rev. Lett.* **89** 270401
- [29] Bender C M 2007 *Rep. Prog. Phys.* **70** 947
- [30] Lee Y C, Hsieh M H, Flammia S T and Lee R K 2014 *Phys. Rev. Lett.* **112** 130404
- [31] Chen S L, Chen G Y and Chen Y N 2014 *Phys. Rev. A* **90** 054301
- [32] Brody D C 2015 *Consistency of PT-symmetric quantum mechanics* arXiv:1508.02190 [quant-ph]
- [33] Leonhardt U 2006 *Science* **312** 1777–80
- [34] Pendry J B, Schurig D and Smith D R 2006 *Science* **312** 1780–2
- [35] Deschamps G A 1971 *Electron. Lett.* **7** 684–5
- [36] Felsen L B 1976 *Symp. Math.* **18** 39–56
- [37] Chapman S J, Lawry J M H, Ockendon J R and Tew R H 1999 *SIAM Rev.* **41** 417–509
- [38] Kravtsov Y A, Forbes G and Asatryan A 1999 *Theory and applications of complex rays (Progress in Optics vol 39)* ed E Wolf (Amsterdam: Elsevier) 1–62
- [39] Chew W C, Jin J M and Michielssen E 1997 *Microwave Opt. Technol. Lett.* **15** 363–9
- [40] Popa B I and Cummer S A 2011 *Phys. Rev. A* **84** 063837
- [41] Castaldi G, Gallina I, Galdi V, Alù A and Engheta N 2011 *J. Opt.* **13** 024011
- [42] Horsley S A R, King C G and Philbin T G 2015 *Wave propagation in complex coordinates* arXiv:1508.04461 [physics.class-ph]
- [43] Post E J 1997 *Formal Structure of Electromagnetics: General Covariance and Electromagnetics* (New York: Dover Publications)
- [44] Gallina I, Castaldi G, Galdi V, Alù A and Engheta N 2010 *Phys. Rev. B* **81** 125124
- [45] Siegman A E 1986 *Lasers* (Mill Valley, CA: University Science Books)
- [46] Pendry J B and Ramakrishna S A 2003 *J. Phys.: Condens. Matter* **15** 6345–64
- [47] Mackay T G and Lakhtakia A 2015 *Phys. Rev. A* **92** 053847
- [48] Maciel J J and Felsen L B 1989 *IEEE Trans. Antennas Propag.* **37** 884–92
- [49] Collin R E 1991 *Field Theory of Guided Waves* (Wiley-IEEE Press)
- [50] Jackson D R and Oliner A 1988 *IEEE Trans. Antennas Propag.* **36** 905–10
- [51] Rahm M, Cummer S A, Schurig D, Pendry J B and Smith D R 2008 *Phys. Rev. Lett.* **100** 063903
- [52] Roberts D A, Rahm M, Pendry J B and Smith D R 2008 *Appl. Phys. Lett.* **93** 251111
- [53] Jiang W X, Cui T J, Ma H F, Yang X M and Cheng Q 2008 *Appl. Phys. Lett.* **93** 221906



- 
- [54] Luo Y, Zhang J, Chen H, Huangfu J and Ran L 2009 *Appl. Phys. Lett.* **95** 193506
- [55] Tichit P H, Burokur S N and de Lustrac A 2009 *J. Appl. Phys.* **105** 104912
- [56] Felsen L B and Marcuvitz N 1994 *Radiation and Scattering of Waves* (New York: Wiley)
- [57] Abramowitz M and Stegun I A 1965 *Handbook of Mathematical Functions: With Formulas Graphs, and Mathematical Tables* (New York: Dover)
- [58] COMSOL Group 2015 *COMSOL Multiphysics* Version 5.0 (COMSOL)